Tunable topological semimetallic phases in Kondo lattice systems

Yen-Wen Lu,[1] Po-Hao Chou,[1] Chung-Hou Chung,[2] and Chung-Yu Mou[1,3,4]

[1]*Center for Quantum Technology and Department of Physics, National Tsing Hua University, Hsinchu 30043, Taiwan 300, Republic of China*

[2]*Electrophysics Department, National Chiao-Tung University, Hsinchu 30010, Taiwan, Republic of China*

[3]*Institute of Physics, Academia Sinica, Nankang 115, Taiwan, Republic of China*

[4]*Physics Division, National Center for Theoretical Sciences, Hsinchu 30013, Taiwan, Republic of China*

(Received 28 September 2018; published 22 January 2019)

We exploit topological semimetallic phases resulting from the Kondo screening in Anderson lattice models. It is shown that by including spin-orbit interactions both in the bulk electrons and in the hybridization between the conduction electrons and electrons in the f orbit, all types of topological semimetallic phases can be realized in Anderson lattice models. Specifically, upon either broken time-reversal symmetry or broken inversion symmetry, we find that either the Weyl semimetallic phase, Dirac semimetallic phase, or nodal-ring semimetallic phases always emerge between insulating phases and can be accessed by tuning either temperature or spin-orbit interaction. For Anderson lattice models with general three-dimensional spin-orbit hybridization between the conduction electrons and electrons in the f orbit, we find that Weyl nodal-ring semimetallic phases emerge between strong and weak topological insulating phases. Furthermore, in the presence of an exchange field, Weyl semimetallic phases form after two Weyl points of charge ± 1 split off from a Dirac point at time-reversal momenta. On the other hand, when the spin-orbit interaction is included in the conduction electron, we find that upon the rotation symmetry being broken with anisotropic hopping amplitudes, a Weyl semimetallic phase emerges with a double Weyl node with charges of ± 2. Furthermore, the Weyl semimetallic phases with charges of ± 2 can be tuned into Weyl semimetallic phases with charges of ± 1 through the inclusion of the Rashba spin-orbit interaction. Our analyses indicate that Anderson lattices with appropriate spin-orbit interactions provide a platform for realizing all types of topological semimetallic phases.

DOI: 10.1103/PhysRevB.99.035141

I. INTRODUCTION

Topological semimetals have recently attracted a lot of attention in condensed-matter physics due to their bulk massless electronic structures and the presence of surface states in specific surfaces [1–4]. Starting from graphene discovered in 2004 [5,6], in which massless two-dimensional (2D) Dirac fermions were realized, several materials that realize three-dimensional (3D) version of semimetals, Dirac semimetals (e.g., Na_3Bi [7], Cd_3As_2 [8,9]) and Weyl semimetals (e.g., TaAs [10–12]), were found subsequently. More recently, massless points that form nodal lines were further found in $PbTaSe_2$ [13] and ZrSiS [14]. In these materials, the conduction and valence bands cross at either discrete points (Dirac or Weyl semimetal [15]) or at lines (nodal line [16] or ring semimetals) in the Brillouin zone (BZ). The crossing points are protected by symmetries [17] and are responsible for a number of novel transport properties (such as the anomalous Hall effect and the chiral magnetic effect) in these materials. While these topological semimetals are usually formed by symmetries with fixed electronic structures, the corresponding semimetallic phase is the critical phase that controls phase transitions between two insulating phases with different topological properties. In particular, this implies that semimetallic phases can be accessed through phase transitions. In the case of discrete massless points, it is known that the mass of the Dirac point controls the transition between the topologically trivial and the topologically nontrivial phases [18]. Right at the point when the mass vanishes, the material is a Dirac semimetal which is at a quantum critical point between the hole Fermi liquid and the electron Fermi liquid [19]. Recently, it was shown that the Kondo screening in the Anderson lattices provides a platform to access the Dirac semimetallic critical point [20]. The semimetallic critical point was also shown to be realized in a Kondo-Heisenberg Hamiltonian with integer filling of electrons [21]. In particular, the electronic structure due to the Kondo screening depends on temperature [22–24], so the Dirac semimetallic phase can also be accessed by tuning temperatures [20]. Indeed, several reports have indicated that tuning temperatures or spin-orbit coupling strength to assess semimetallic phases is feasible experimentally [25–28]. Motivated by these observations, it is therefore appealing to explore possible semimetallic phases that can be accessed by the Kondo screening in Anderson lattices.

In this work, we explore topological semimetallic phases resulting from the Kondo screening in simple cubic Anderson lattices. It is shown that by including appropriate spin-orbit interactions, all types of topological semimetallic phases can be realized in simple cubic Anderson lattices. Specifically, we shall show that upon either broken time-reversal symmetry or broken inversion symmetry, either the Weyl semimetallic phase, Dirac semimetallic phase, or nodal-line semimetallic phases always emerge between insulating phases with different topological properties. Furthermore, these topological

semimetallic phases can be accessed by tuning either temperature or spin-orbit interaction. Our results reveal the unusual interplay between the topology of the electronic structures and the Kondo screening in the strongly correlated Anderson lattices and pave the way for systematically engineering topological semimetals based on Kondo lattice systems.

The rest of the paper is organized as follows. In Sec. II, the generic Anderson lattice model on a simple cubic lattice with spin-orbit interactions is introduced. By using the slave-boson method, the mean-field Hamiltonian is constructed. In Sec. III, we examine the Anderson lattice model without time-reversal symmetry. The resulting Weyl semimetallic phase is inversion symmetric, with Weyl nodes being split off from a Dirac point at time-reversal momenta. In Sec. IV, we show that the Weyl nodal-ring semimetallic phase generally emerges when the inversion symmetry is broken in the Anderson lattice model with general hybridization between the conduction electron and the f electron. Section V is devoted to the investigation of the Anderson lattice without inversion symmetry through the bulk spin-orbit interaction. It is shown that depending on the nature of spin-orbit interaction in hybridization, the emergent Weyl semimetallic phase can host Weyl nodes with monopole charges being ± 1 or double Weyl nodes with charges being ± 2. Finally, in Sec. VI, we conclude and discuss possible effects due to fluctuations that go beyond the mean-field theory.

II. THEORETICAL MODEL

We start by considering the generic Anderson lattice model that includes spin-orbit interactions on a simple cubic lattice. The model that describes the effects of Kondo screening can be generally described by the following Hamiltonian:

$$H = \sum_{\mathbf{k}\sigma} \left(\xi_{\mathbf{k}} c^\dagger_{\mathbf{k}\sigma} c_{\mathbf{k}\sigma} + \xi^d_{\mathbf{k}} d^\dagger_{\mathbf{k}\sigma} d_{\mathbf{k}\sigma}\right) + H_{SO} + \sum_{\mathbf{k}\sigma\sigma'} \left(V^{\sigma\sigma'}_{\mathbf{k}} c^\dagger_{\mathbf{k}\sigma} d_{\mathbf{k}\sigma'} + \text{H.c.}\right) + U \sum_i n^d_{i\uparrow} n^d_{i\downarrow}. \quad (1)$$

Here $c^\dagger_{\mathbf{k}\sigma}$ and $d^\dagger_{\mathbf{k}\sigma}$ create conduction and more localized electrons in the f orbit with momentum $\mathbf{k}$ and spin σ, respectively. $\xi_{\mathbf{k}}$ is the energy dispersion due to the nearest hopping amplitude t and is equal to $\varepsilon_{\mathbf{k}} - \mu$, with $\varepsilon_{\mathbf{k}} = -2t \sum_{i=x,y,z} \cos k_i$ and μ being the chemical potential. $\xi^d_{\mathbf{k}} = \varepsilon_d - \eta\varepsilon_{\mathbf{k}} - \mu$ characterizes the narrow band formed by d electrons, with η being the bandwidth and ε_d being the relative shift of the band center. H_{SO} is the spin-orbit interaction and is generally given by

$$H_{SO} = \sum_{\mathbf{k}\sigma\sigma'} \left(2\lambda^{\sigma\sigma'}_{\mathbf{k}} c^\dagger_{\mathbf{k}\sigma} c_{\mathbf{k}\sigma'} + 2\bar{\lambda}^{\sigma\sigma'}_{\mathbf{k}} d^\dagger_{\mathbf{k}\sigma} d_{\mathbf{k}\sigma'}\right), \quad (2)$$

where $\lambda^{\sigma\sigma'}_{\mathbf{k}}$ and $\bar{\lambda}^{\sigma\sigma'}_{\mathbf{k}}$ can be either Dirac-type spin-orbit interaction, $\boldsymbol{\sigma} \cdot \sin \mathbf{k}$ [22], or Rashba-type interaction, $\hat{z} \cdot \boldsymbol{\sigma} \times \sin \mathbf{k}_{2D}$. Here $\sin \mathbf{k}$ denotes $(\sin k_x, \sin k_y, \sin k_z)$, while $\sin \mathbf{k}_{2D}$ denotes $(\sin k_x, \sin k_y, 0)$. $\mathbf{V}_{\mathbf{k}}$ is the hybridization matrix (taken to be real) that describes the hybridization between c and d electrons and will be taken in the form $v_0 + \mathbf{V}_{SO}(\mathbf{k})$, with $\mathbf{V}_{SO}(\mathbf{k})$ being due to spin-orbit interaction and being linear in $\mathbf{k}$ [20,22]. Finally, U describes the Hubbard repulsion between d electrons.

In order to access the electronic structures in the large-U limit, the slave-boson method is employed. In this method, the creation operators of d electrons are represented by $d^\dagger_{i\sigma} = f^\dagger_{i\sigma} b_i$, where $f_{i\sigma}$ and b_i are the spinon and holon operators, respectively, which satisfy the constraint $\sum_\sigma f^\dagger_{i\sigma} f_{i\sigma} + b^\dagger_i b_i = 1$. This constraint can be satisfied by introducing a Lagrangian field λ_i. In the low-temperature limit, we apply the mean-field approximation by assuming holons condense, so that $\langle b_i \rangle = \langle b^\dagger_i \rangle = r$ and λ_i is replaced by its mean value λ. Consequently, the Hamiltonian becomes $H_M = \sum_{\mathbf{k}\sigma} (c_{\mathbf{k}\sigma}, f_{\mathbf{k}\sigma})^\dagger h_{\mathbf{k}} (c_{\mathbf{k}\sigma}, f_{\mathbf{k}\sigma}) + N\lambda(r^2 - 1)$, with

$$h_{\mathbf{k}} = \begin{pmatrix} \xi_{\mathbf{k}} \mathbb{1} + \lambda_{\mathbf{k}} & \widetilde{V}_{\mathbf{k}} \\ \widetilde{V}_{\mathbf{k}} & \tilde{\xi}^d_{\mathbf{k}} \mathbb{1} + r^2 \bar{\lambda}_{\mathbf{k}} \end{pmatrix}. \quad (3)$$

Here $\widetilde{V}_{\mathbf{k}} = r V_{\mathbf{k}}$, $\tilde{\xi}^d_{\mathbf{k}} = (\varepsilon_d + \lambda) - \eta r^2 \varepsilon_{\mathbf{k}} - \mu$, N is number of lattice points, and we have made use of $\sum_\sigma f^\dagger_{i\sigma} f_{i\sigma} = \sum_\sigma d^\dagger_{i\sigma} d_{i\sigma}$. Given the Hamiltonian $h_{\mathbf{k}}$, λ and r are determined by minimizing the free energy with respect to λ and r. As a result, we find that λ and r can be determined by solving the following mean-field equations self-consistently:

$$\frac{1}{N} \sum_{\mathbf{k}\sigma} \langle f^\dagger_{\mathbf{k}\sigma} f_{\mathbf{k}\sigma} \rangle + r^2 = 1, \quad (4)$$

$$\frac{1}{N} \sum_{\mathbf{k}\sigma\sigma'} \left[\text{Re}\left(V^{\sigma\sigma'}_{\mathbf{k}} \langle c^\dagger_{\mathbf{k}\sigma} f_{\mathbf{k}\sigma'} \rangle\right) - r\left(2\bar{\lambda}^{\sigma\sigma'}_{\mathbf{k}} + \eta\varepsilon_{\mathbf{k}} \delta_{\sigma\sigma'}\right) \langle f^\dagger_{\mathbf{k}\sigma} f_{\mathbf{k}\sigma'} \rangle\right] + r\lambda = 0. \quad (5)$$

For further analysis of the energy band, it is convenient to rewrite $\xi_{\mathbf{k}} = -\mu_{\mathbf{k}} + m_{\mathbf{k}}$ and $\tilde{\xi}^d_{\mathbf{k}} = -\mu_{\mathbf{k}} - m_{\mathbf{k}}$, with $\mu_{\mathbf{k}} = \mu - [(1 - \eta r^2)\varepsilon_{\mathbf{k}} + \varepsilon_d + \lambda]/2$ and $m_{\mathbf{k}} = [(1 + \eta r^2)\varepsilon_{\mathbf{k}} - \varepsilon_d - \lambda]/2$, so that the Hamiltonian can be cast in the tensor-product form as

$$h_{\mathbf{k}} = -\mu_{\mathbf{k}} \tau_0 \otimes \sigma_0 + m_{\mathbf{k}} \tau_z \otimes \sigma_0 + \tau_x \otimes \widetilde{V}_{\mathbf{k}} + (\tau_0 + \tau_z) \otimes \lambda_{\mathbf{k}} + r^2 (\tau_0 - \tau_z) \otimes \bar{\lambda}_{\mathbf{k}}, \quad (6)$$

where $\tau_0 = \sigma_0 = \mathbb{1}$, $\boldsymbol{\tau} = (\tau_x, \tau_y, \tau_z)$ are the Pauli matrices that act on the orbital degree (c or f) of freedom, and $\boldsymbol{\sigma} = (\sigma_x, \sigma_y, \sigma_z)$ act on the real spin. In the above orbital and spin basis, the corresponding time-reversal operator Θ and inversion operator P are given by

$$\Theta = i\tau_0 \otimes \sigma_y K, \quad P = \tau_z \otimes \sigma_0, \quad (7)$$

where K stands for complex conjugation [15]. It is then straightforward to see that in the absence of spin-orbit interactions ($H_{SO} = 0$) and when $\mathbf{V}_{\mathbf{k}} = \mathbf{V}_{SO}(\mathbf{k})$, the Hamiltonian $h_{\mathbf{k}}$ satisfies $\Theta h_{\mathbf{k}} \Theta^{-1} = h_{-\mathbf{k}}$ and $P h_{\mathbf{k}} P^{-1} = h_{-\mathbf{k}}$. Hence the Anderson lattice model without spin-orbit interactions is both time reversal symmetric and inversion symmetric. It has been shown that this system supports stable finite-temperature Dirac points protected by both time-reversal symmetry (TRS) and inversion symmetry (IS) [20].

III. INVERSION-SYMMETRIC WEYL SEMIMETALLIC PHASE

We first consider the Weyl semimetallic phase when the Anderson lattice is inversion symmetric. In this case, we take

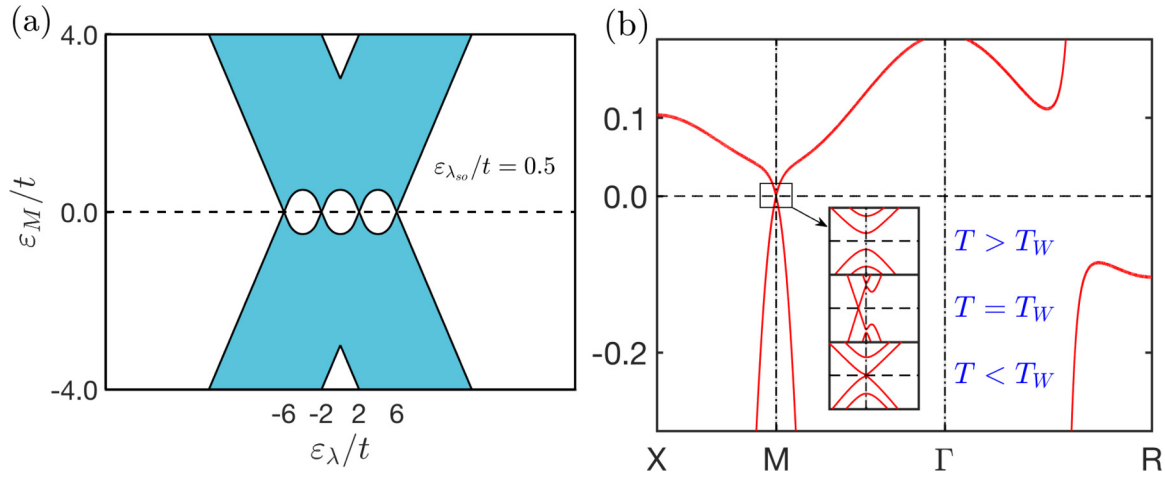

FIG. 1. (a) Phase diagram of the Anderson lattice model with an external magnetic field. Here $\varepsilon_\lambda \equiv (\varepsilon_d + \lambda)/(1+\eta r^2)$, $\varepsilon_{\lambda_{so}} \equiv r\lambda_{so}/(1+\eta r^2)$, and $\varepsilon_M \equiv M/(1+\eta r^2)$. The shaded regime is the Weyl semimetallic phase, while white regimes are insulating phases with gaps in electronic structures. When $\varepsilon_M = 0$, the gapless phases at $\varepsilon_\lambda/t = -6, -2, 2, 6$ are Dirac semimetallic phases with corresponding Dirac points being at time-reversal momenta Γ, X, M, R, respectively. (b) Emergence of a finite-temperature Weyl point that splits off from the M point. Here $t = 1$, $\lambda_{so} = 0.14$, $\eta = 0.05$, $\varepsilon_d = 1.837$, $M_z = 0.001$. The transition temperature when the Kondo insulator becomes a Weyl semimetal occurs at $T_W = 0.03$.

$H_{SO} = 0$, and the hybridization matrix takes the following form:

$$\mathbf{V}_\mathbf{k} = 2\lambda_{so}\boldsymbol{\sigma}\cdot\sin\mathbf{k}. \tag{8}$$

The resulting Anderson model describes SmB_6, in which v_0 vanishes due to the odd parity of the f orbits [22], so that the spin-orbit interaction λ_{so} dominates. To obtain a Weyl semimetallic phase, we further include exchange fields that break the time-reversal symmetry, so that the following additional Hamiltonian is included:

$$H^M_\mathbf{k} = \sum_\mathbf{k} \mathbf{M}_c\cdot(c^\dagger_{\mathbf{k}\alpha}\boldsymbol{\sigma}_{\alpha\beta}c_{\mathbf{k}\beta}) + \mathbf{M}_f\cdot(f^\dagger_{\mathbf{k}\alpha}\boldsymbol{\sigma}_{\alpha\beta}f_{\mathbf{k}\beta}). \tag{9}$$

Here $\mathbf{M}_c$ and $\mathbf{M}_f$ are exchange fields for the conduction and d electrons, respectively, and we have made use of the relation $d^\dagger_{\mathbf{k}\alpha}\boldsymbol{\sigma}_{\alpha\beta}d_{\mathbf{k}\beta} = f^\dagger_{\mathbf{k}\alpha}\boldsymbol{\sigma}_{\alpha\beta}f_{\mathbf{k}\beta}$. For simplicity, we shall set $\mathbf{M}_c = \mathbf{M}_f = \mathbf{M} = M_z\hat{z}$. The resulting Hamiltonian is given by

$$h_\mathbf{k} = -\mu_\mathbf{k}\tau_0\otimes\sigma_0 + m_\mathbf{k}\tau_z\otimes\sigma_0 + 2r\lambda_{so}\tau_x\otimes\boldsymbol{\sigma}\cdot\sin\mathbf{k} + M_z\tau_0\otimes\sigma_z. \tag{10}$$

Clearly, we have $\Theta\mathcal{H}_\mathbf{k}\Theta^{-1} \neq \mathcal{H}_{-\mathbf{k}}$ and $P\mathcal{H}_\mathbf{k}P^{-1} = \mathcal{H}_{-\mathbf{k}}$. Hence the time-reversal symmetry of the system is broken, while the inversion symmetry still holds. The energy spectrum has an analytic form and is given by

$$E^{(\alpha,\beta)}_\mathbf{k} = -\mu_\mathbf{k} + \alpha\sqrt{\left(\sqrt{m^2_\mathbf{k} + 4r^2\lambda^2_{so}\sin^2 k_z} + \beta M_z\right)^2 + 4r^2\lambda^2_{so}\sin^2\mathbf{k}_{2D}}, \tag{11}$$

where $\alpha = (+,-)$ and $\beta = (+,-)$ are indices for signs. It is clear that the branch $E^{(\alpha,+)}_\mathbf{k}$ is always gapful when $M_z > 0$, while the branch $E^{(\alpha,-)}_\mathbf{k}$ is always gapful when $M_z < 0$. Obviously, gapless phases are determined by the condition $E^{(+,-)}_\mathbf{k} - E^{(-,-)}_\mathbf{k} = 2\sqrt{(\sqrt{m^2_\mathbf{k} + 4r^2\lambda^2_{so}\sin^2 k_z} - M_z)^2 + 4r^2\lambda^2_{so}\sin^2\mathbf{k}_{2D}} = 0$. Hence by setting $\sin^2\mathbf{k}_{2D} = 0$ and $\sqrt{m^2_{\mathbf{k}_w} + 4r^2\lambda^2_{so}\sin^2 k_{w_z}} - M_z = 0$, we determine all possible gapless momenta $\mathbf{k}_w = (k_{w_x}, k_{w_y}, k_{w_z})$, which satisfy

$$\left(\varepsilon_{\mathbf{k}_w} - \varepsilon_\lambda\right)^2 + 16\varepsilon^2_{\lambda_{so}}\sin^2 k_{w_z} = 4\varepsilon^2_M, \tag{12}$$

where relevant parameters are given by $\varepsilon_\lambda \equiv (\varepsilon_d + \lambda)/(1+\eta r^2)$, $\varepsilon_{\lambda_{so}} \equiv r\lambda_{so}/(1+\eta r^2)$, and $\varepsilon_M \equiv M_z/(1+\eta r^2)$. It is clear to see that ε_λ, $\varepsilon_{\lambda_{so}}$, and ε_M are the effective parameters that tune the Kondo insulator into different phases. Solutions to Eq. (12) give rise to phase diagrams shown in Fig. 1(a), where the gapless Weyl semimetallic phase is shown as the shaded regime. Furthermore, by solving the mean-field equations, Eqs. (4) and (5), we find that it is possible to tune the Kondo insulator so that it becomes a Weyl semimetal at finite temperatures. As shown in Fig. 1(b), the transition occurs at $T_W = 0.03$ when parameters are taken to be $t = 1$, $\lambda_{so} = 0.14$, $\eta = 0.05$, $\varepsilon_d = 1.837$, $M_z = 0.001$.

Here we further analyze the charge associated with the Weyl point located at $\mathbf{k}_w = (0, \pi, k_{w_z})$. Near the nodal point, the linearized Hamiltonian can be recast into the form

$$h_{\mathbf{k}_w+\mathbf{q}} = \begin{pmatrix} \xi^+_{\mathbf{k}_w+\mathbf{q}} & 0*\mathbb{1}_{2\times2} \\ 0*\mathbb{1}_{2\times2} & \xi^-_{\mathbf{k}_w+\mathbf{q}} \end{pmatrix}, \tag{13}$$

with

$$\xi^\pm_{\mathbf{k}_w+\mathbf{q}} \equiv -\mu_{\mathbf{k}_w+\mathbf{q}}\tau_0 + \left(\widetilde{m}_{\mathbf{k}_w+\mathbf{q}} \pm M_z\right)\tau_z + 2r\lambda_{so}q_\pm\tau_+ + \text{H.c.}, \tag{14}$$

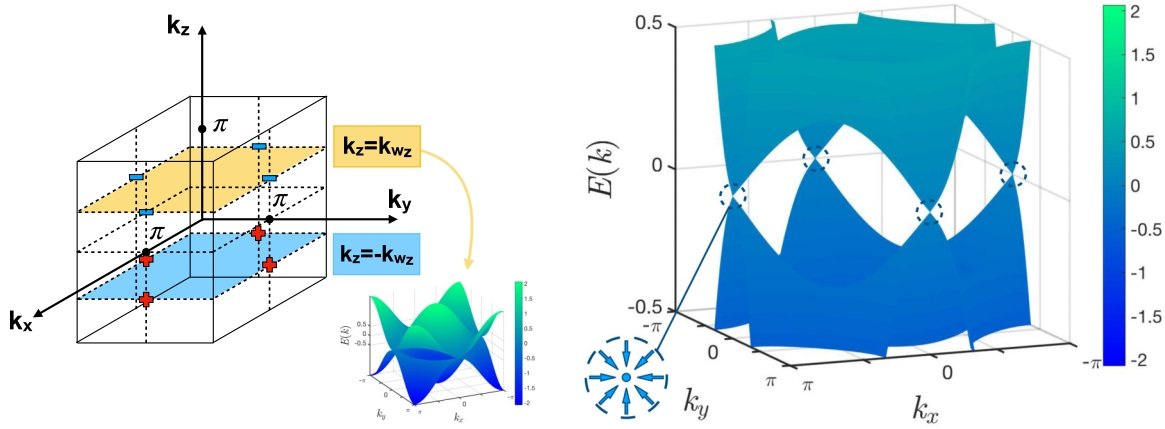

FIG. 2. Sketch of the distribution of Weyl nodes in the first Brillouin zone. The monopole charges of each Weyl nodes are denoted by $-$ or $+$. Weyl nodes move along the dashed lines when the temperature changes. Notice that in order to display Weyl nodes clearly, here $E(k)$ does not include the effective chemical potential $\mu_{\mathbf{k}}$.

where $\tau_\pm = (\tau_x \pm i\tau_y)/2$, $q_\pm = q_x \pm iq_y$, and $\tilde{m}_{\mathbf{k}_w+\mathbf{q}} = \sqrt{m^2_{\mathbf{k}_w+\mathbf{q}} + 4r^2\lambda^2_{so}(q_z \cos k_{w_z})}$. It is clear that $\xi^+_{\mathbf{k}_w+\mathbf{q}}$ is always gapful, while $\xi^-_{\mathbf{k}_w+\mathbf{q}}$ can be tuned to a gapless regime. From the linearized Hamiltonian, we identify the net monopole charge associated with the Weyl node at $(0, \pi, k_{w_z})$ is -1 [29]. A similar analysis allows one to identify all charges of Weyl nodes. This is sketched in Fig. 2.

IV. WEYL NODAL-RING SEMIMETALLIC PHASE

In this section, we demonstrate that the Weyl nodal-ring semimetallic phases emerge in the Anderson lattice model when inversion symmetry is broken. In this case, we take $H_{SO} = 0$, and the hybridization matrix takes the following form [20]:

$$\mathbf{V}_{\mathbf{k}} = v_0 + 2\lambda_{so}\boldsymbol{\sigma} \cdot \sin \mathbf{k}. \tag{15}$$

After applying the slave-boson approximation, the mean-field Hamiltonian is given by

$$\begin{aligned} h_{\mathbf{k}} = &-\mu_{\mathbf{k}}\tau_0 \otimes \sigma_0 + m_{\mathbf{k}}\tau_z \otimes \sigma_0 \\ &+ r\tau_x \otimes (v_0\sigma_0 + 2\lambda_{so}\boldsymbol{\sigma} \cdot \sin \mathbf{k}). \end{aligned} \tag{16}$$

The energy spectrum to $h_{\mathbf{k}}$ has an analytic form and is given by

$$E^{(\alpha,\beta)}_{\mathbf{k}} = -\mu_{\mathbf{k}} + \alpha\sqrt{m^2_{\mathbf{k}} + r^2(v_0 + 2\beta\lambda_{so}\sqrt{\sin^2 \mathbf{k}})^2}, \tag{17}$$

where α and β are $+$ or $-$. Here it is clear that the gap is determined by $E^{(+,\beta)}_{\mathbf{k}} - E^{(-,\beta)}_{\mathbf{k}} = 2\sqrt{m^2_{\mathbf{k}} + r^2(v_0 + 2\beta\lambda_{so}\sqrt{\sin^2 \mathbf{k}_{3D}})^2}$. Obviously, when $\beta = +$, $E^{(\alpha,\beta)}_{\mathbf{k}}$ remains gapful. Furthermore, gapless points $\mathbf{k}_0$ are determined by setting $m_{\mathbf{k}_0} = 0$ and $v_0 - 2\lambda_{so}\sqrt{\sin^2 \mathbf{k}_0} = 0$. These two equations are equivalent to

$$\sum_{i=x,y,z} \cos k_i = -\frac{\varepsilon_\lambda}{2t}, \quad \sum_{i=x,y,z} \cos^2 k_i = 3 - \left(\frac{v_0}{2\lambda_{so}}\right)^2. \tag{18}$$

The solution, $u_i = \cos k_i$, to the second equation in Eq. (18) forms a sphere with radius $\sqrt{u_x^2 + u_y^2 + u_z^2}$, equal to $\sqrt{3 - (v_0/2\lambda_{so})^2}$, while the first equation represents a plane. The distance between the center of the sphere and the plane is given by $|\varepsilon_\lambda/2\sqrt{3}t|$, so that Eq. (18) has solutions only if $|\varepsilon_\lambda/2\sqrt{3}t| \leqslant \sqrt{3 - (v_0/2\lambda_{so})^2}$. The solutions of Eq. (18) form curves illustrated as the boundaries of the shaded area in Fig. 3(a). Right at the boundary, $|\varepsilon_\lambda/2\sqrt{3}t| = \sqrt{3 - (v_0/2\lambda_{so})^2}$, the plane and sphere touch at a point, which gives rises to Weyl nodes. The system is thus a Weyl semimetal. However, when $|\varepsilon_\lambda/2\sqrt{3}t| < \sqrt{3 - (v_0/2\lambda_{so})^2}$, the intersection of a plane and a sphere is a ring in k space. Hence, instead of Weyl semimetallic phases, we find that Weyl nodal-ring semimetallic phases emerge inside the shaded regime in Fig. 3(a).

The Weyl nodal ring lies on the surface defined by $m_{\mathbf{k}} = 0$. Following Ref. [15], near the center of the ring on the surface, by performing the expansion of the wave vector in the local frame to linear terms and removing the smooth energy background term, we find that the effective Hamiltonian is given by

$$h_{\text{eff}}(\mathbf{k}') = rv_0\tau_x \otimes \sigma_0 + 2r\lambda_{so}\tau_x \otimes (\sigma_x k'_x + \sigma_z k'_z), \tag{19}$$

where $\mathbf{k}' = (k'_x, k'_y, k'_z)$, with k'_x and k'_z being the components parallel and perpendicular to the surface defined by $m_{\mathbf{k}} = 0$, respectively. Here the local coordinates are chosen such that the component parallel to the surface defined by $m_{\mathbf{k}} = 0$ is aligned with the k'_x axis. The Hamiltonian h_{eff} is mirror symmetric,

$$M^{-1}h_{\text{eff}}(k'_x, k'_y, -k'_z)M = h_{\text{eff}}(k'_x, k'_y, k'_z), \tag{20}$$

where $M = \tau_x \otimes i\sigma_x$ is the corresponding representation of the mirror symmetry operator. The system is thus mirror symmetric with respect to the surface defined by $m_{\mathbf{k}} = 0$. Since the inversion symmetry is broken when v_0 is nonvanishing, the Weyl nodal ring emerges as the consequence of the presence of mirror symmetry and the broken inversion symmetry [30]. In addition, the effective Hamiltonian is time reversal invariant and has particle-hole symmetry, with the charge conjugation being given by $C = -\tau_y \otimes i\sigma_y K$. The nodal ring is protected by these symmetries and belong to the class CII, with R_{+-} defined in Ref. [31].

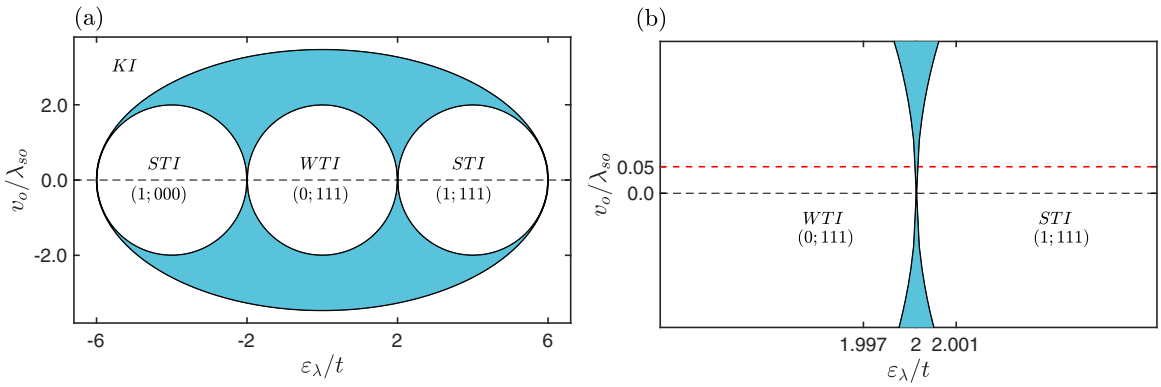

FIG. 3. (a) Topological phase diagram in the presence of constant hybridization v_0 between c and f electrons; shaded regimes indicate gapless phases, while white regimes are insulating phases, labeled by a strong topological insulator (STI), weak topological insulator (WTI), and Kondo insulator (KI) when the valence bands are filled [20]. Here $\varepsilon_\lambda \equiv \frac{\varepsilon_d+\lambda}{1+\eta r^2}$ and $(\nu_0;\nu_1,\nu_2,\nu_3)$ are topological indices. (b) The phase transition path (the red dashed line) in the phase diagram with $t = 1$, $\varepsilon_d = 1.724$, $v_0 = 0.01$, $\lambda_{so} = 0.2$. When the temperature increases from $T = 0.02$ to $T = 0.04$, the Anderson lattice goes through Weyl nodal-ring semimetallic phases.

The Anderson lattice is tunable in temperature. In Fig. 3(b), we demonstrate that finite-temperature phase transitions between a strong topological insulating phase (STI) and a weak topological insulating phase (WTI) through the Weyl nodal-ring semimetallic phase can be achieved by changing temperature. By solving the corresponding self-consistent equations, Eqs. (4) and (5), we find that there is a phase transition from STI ($\varepsilon_\lambda/t = 2.001$, $T = 0.02$) to WTI ($\varepsilon_\lambda/t = 1.997$, $T = 0.04$) through the Weyl nodal-ring semimetallic phase ($\varepsilon_\lambda/t = 2$, $T = 0.03$), as illustrated by the red dashed line in Fig. 3(b).

V. TIME-REVERSAL-SYMMETRIC WEYL SEMIMETALLIC PHASES

In this section, we explore the possibility of forming the Weyl semimetallic phases in the Anderson lattice that are time reversal symmetric. For this purpose, the Anderson lattice model must break the inversion symmetry. In addition, the emergence of Weyl semimetallic phases requires certain crystal symmetries, in which 3D rotational symmetry breaks down to axial symmetries [29]. Therefore, to realize the Weyl semimetallic phase with time-reversal symmetry, the Anderson lattice is assumed to have layered structure with axial symmetry. The energy dispersion $\varepsilon_{\mathbf{k}}$ is given by

$$\varepsilon_{\mathbf{k}} = -2t \sum_{i=x,y,z} a_i \cos k_i, \tag{21}$$

where a_i represents the relative hopping strength of each direction and we set $0 < a_z < a_y < a_x = 1$. In addition, the hybridization matrix takes the two-dimensional form with either

$$\mathbf{V}^1_{\mathbf{k}} = 2\lambda_{so}\boldsymbol{\sigma} \cdot \sin \mathbf{k}_{2D} \tag{22}$$

or the Rashba spin-orbit interaction

$$\mathbf{V}^2_{\mathbf{k}} = 2\lambda_{Ra}\hat{z} \cdot \boldsymbol{\sigma} \times \sin \mathbf{k}_{2D}, \tag{23}$$

where λ_{so} and λ_{Ra} describe the strength of different forms of 2D spin-orbit interactions.

We shall first consider $\mathbf{V}^1_{\mathbf{k}}$. For bulk spin-orbit interactions, in the simplest situation, both c and d electrons are governed by the same bulk spin-orbit interactions, which are characterized by setting $\lambda_{\mathbf{k}} = \boldsymbol{\sigma} \cdot \sin \mathbf{k}$ and $r^2\bar{\lambda}_{\mathbf{k}} = \boldsymbol{\sigma} \cdot \sin \mathbf{k}$ in Eq. (6). As a result, the total Hamiltonian is given by

$$\begin{aligned} h_{\mathbf{k}} = &-\mu_{\mathbf{k}}\tau_0 \otimes \sigma_0 + m_{\mathbf{k}}\tau_z \otimes \sigma_0 + 2r\lambda_{so}\tau_x \otimes \boldsymbol{\sigma} \cdot \sin \mathbf{k}_{2D} \\ &+ \tilde{\lambda}_{so}(\tau_0 + \tau_z) \otimes \boldsymbol{\sigma} \cdot \sin \mathbf{k} + \tilde{\lambda}_{so}(\tau_z - \tau_0) \otimes \boldsymbol{\sigma} \cdot \sin \mathbf{k}, \end{aligned} \tag{24}$$

where $\tilde{\lambda}_{so}$ describes the strength of the bulk spin-orbit interaction. In this case, the energy spectrum of Eq. (24) has an analytic form, which is given by

$$E^{(\alpha,\beta)}_{\mathbf{k}} = -\mu_{\mathbf{k}} + \beta\sqrt{m^2_{\mathbf{k}} + 4r^2\lambda^2_{so}\sin^2 \mathbf{k}_{2D} + 4\tilde{\lambda}^2_{so}\sin^2 \mathbf{k} + 4\alpha\tilde{\lambda}_{so}\sqrt{m^2_{\mathbf{k}}\sin^2 \mathbf{k} + 4r^2\lambda^2_{so}|\sin \mathbf{k} \times \sin \mathbf{k}_{2D}|^2}}, \tag{25}$$

where α and β equal to ± 1. It is clear that $E^{(+,\beta)}_{\mathbf{k}}$ remains gapful at all times. Hence the gapless phase occurs in the branch $\alpha = -1$. The gapless point occurs by requiring $|\sin \mathbf{k} \times \sin \mathbf{k}_{2D}|$ to reach its maximum value, i.e., $\sin \mathbf{k} \cdot \sin \mathbf{k}_{2D} = 0$ and, at the same time, $\sin^2 \mathbf{k}_{2D} = 0$. As a result, we find $m_{\mathbf{k}} - 2\tilde{\lambda}_{so}\sqrt{\sin^2 \mathbf{k}}_{=0}$ has to be satisfied. The condition for the occurrence of the Weyl semimetallic phase is then given by

$$(\varepsilon_{\mathbf{k}_w} - \varepsilon_\lambda)^2 = 4\varepsilon^2_{\tilde{\lambda}_{so}}\sin^2 k_{w_z}, \tag{26}$$

where $\varepsilon_{\tilde{\lambda}_{so}} \equiv \tilde{\lambda}_{so}/(1 + \eta r^2)$. In the isotropic limit where $a_z = a_y = a_x = 1$, solutions to Eq. (26) form the boundary curve

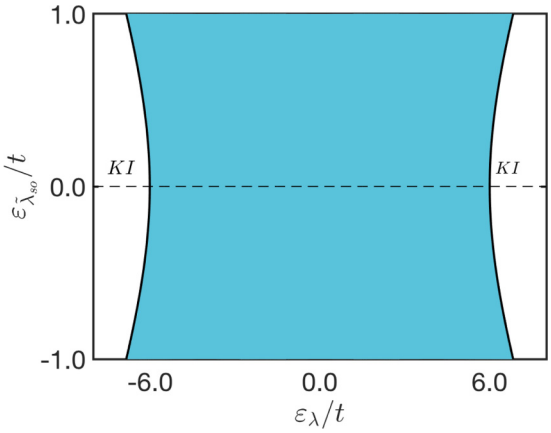

FIG. 4. Topological phase diagram in the presence of the bulk spin-orbit interaction in c and d electrons with equal strength. Here the hopping amplitude is isotropic, with $a_z = a_y = a_x = 1$. The shaded regime is the Weyl semimetallic phases, while the white regime is the Kondo insulating phase.

between the Weyl semimetallic phase and the Kondo insulating phase, as illustrated in Fig. 4.

The monopole charge of the Weyl node in this case can be analyzed by linearizing the Hamiltonian near the node. Taking the Weyl node at point X, $\mathbf{k}_w = (0, \pi, k_{w_z})$, as an example, after linearization, the Hamiltonian can be rewritten in the form of Eq. (13) with

$$\xi^{\pm}_{\mathbf{k}_w+\mathbf{q}} = \big(-\mu_{\mathbf{k}_w+\mathbf{q}} \pm K_z\big)\tau_0 + \big(m_{\mathbf{k}_w+\mathbf{q}} \pm K_z\big)\tau_z + \frac{4r\lambda_{so}}{\sin k_{w_z}} q_{\pm}^2 \tau_+ + \text{H.c.}, \tag{27}$$

where $K_z = 2\tilde{\lambda}_{so}(q_z \cos k_{w_z} + \sin k_{w_z})$. Clearly, $\xi^{+}_{\mathbf{k}_w+\mathbf{q}}$ is gapful, while $\xi^{-}_{\mathbf{k}_w+\mathbf{q}}$ can be tuned into gapless phases. The monopole charge corresponding to Eq. (27) is -2 [29]. Hence the monopole charges of Weyl nodes in the Weyl semimetallic phase shown in Fig. 4 are ± 2.

In real materials, bulk spin-orbit interactions in c and d electrons are generally not of the same strength. Therefore we consider the relative strength in the spin-orbit interaction of d electrons. After applying the mean-field slave-boson approximation, the Hamiltonian is given by

$$h_{\mathbf{k}} = -\mu_{\mathbf{k}}\tau_0 \otimes \sigma_0 + m_{\mathbf{k}}\tau_z \otimes \sigma_0 + 2r\lambda_{so}\tau_x \otimes \boldsymbol{\sigma} \cdot \sin \mathbf{k}_{2D} + \tilde{\lambda}_{so}(\tau_0 + \tau_z) \otimes \boldsymbol{\sigma} \cdot \sin \mathbf{k}_{3D} + \eta r^2 \tilde{\lambda}_{so}(\tau_z - \tau_0) \otimes \boldsymbol{\sigma} \cdot \sin \mathbf{k}_{3D}. \tag{28}$$

Unfortunately, the energy spectrum to $h_{\mathbf{k}}$ in Eq. (28) no longer has an analytic form. However, because the system is axial symmetric with respect to the z axis and the gapless phase occurs when $\sin^2 \mathbf{k}_{2D} = 0$, the relevant spectrum for the Weyl semimetallic phase is determined by the spectrum along the z axis. As we can see, along the z axis, $E^{(\alpha,+)}(0, 0, k_z)$ remains gapped. The possible gapless phases are thus determined by $E^{(-,+)}_{\mathbf{k}} - E^{(-,-)}_{\mathbf{k}}|_{\mathbf{k}=(0,0,k_z)} = 2[m_{k_z} - \tilde{\lambda}_{so}(1 + \eta r^2) \sin k_z]$. Hence $m_{k_z} = 2\tilde{\lambda}_{so}(1 + \eta r^2) \sin k_z$ and $\sin^2 \mathbf{k}_{2D} = 0$ determine all possible gapless phases with the corresponding nodal point $\mathbf{k}_w = (0, 0, k_{w_z})$. The condition for the Weyl semimetallic phase is then given by

$$\big(\varepsilon_{\mathbf{k}_w} - \varepsilon_\lambda\big)^2 = 4\tilde{\lambda}_{so}^2 \sin^2 k_{w_z}. \tag{29}$$

By including the anisotropy of hopping amplitudes with $\varepsilon_{\mathbf{k}} = -2t \sum_{i=x,y,z} a_i \cos k_i$ and $0 < a_z < a_y < a_x = 1$, solutions to Eq. (29) form the boundary curve between the Weyl semimetallic phase and insulating phases, as illustrated in Fig. 5(a). Here insulating phases are WTI or STI, labeled by the corresponding topological indices [32]. Furthermore, by solving the mean-field equations, Eqs. (4) and (5), we find that it is possible to tune the Kondo insulator across Weyl semimetallic phases at finite temperatures. As illustrated in Fig. 5(b), the transition occurs at $T_W = 0.03$ when parameters are taken to be $t = 1$, $\lambda_{so} = 0.2$, $\eta = 0.05$, $\varepsilon_d = 0.705$, $\tilde{\lambda}_{so} = 0.001$, $a_y = 0.5$, and $a_z = 0.001$. It is seen that the critical temperature for the emergence of Weyl nodes is $T_W = 0.03$. In addition, as indicated by the linearized Hamiltonian in Eq. (27), the net monopole charge associated with each Weyl node is ± 2. The distribution of Weyl nodes is sketched in Fig. 6.

We now consider the Rashba spin-orbit hybridization interaction $\mathbf{V}^2_{\mathbf{k}}$. In this case, we shall show that instead of ± 2, the monopole charge associated with the Weyl node is ± 1. In this case, the Hamiltonian becomes

$$h_{\mathbf{k}} = -\mu_{\mathbf{k}}\tau_0 \otimes \sigma_0 + m_{\mathbf{k}}\tau_z \otimes \sigma_0 + 2r\lambda_{Ra}\tau_x \otimes \boldsymbol{\sigma} \cdot \sin \mathbf{k}_{Ra} + \tilde{\lambda}_{so}(\tau_0 + \tau_z) \otimes \boldsymbol{\sigma} \cdot \sin \mathbf{k} + \eta r^2 \tilde{\lambda}_{so}(\tau_z - \tau_0) \otimes \boldsymbol{\sigma} \cdot \sin \mathbf{k}, \tag{30}$$

where we have denoted $\sin \mathbf{k}_{Ra} = \sin \mathbf{k}_{2D} \times \hat{z}$. In comparison to the Hamiltonian corresponding to $\mathbf{V}^1_{\mathbf{k}}$, it is clear that λ_{Ra} and $\mathbf{k}_{Ra}$ simply replace λ_{so} and $\mathbf{k}_{2D}$. However, because $\sin \mathbf{k}_{Ra} \cdot \sin \mathbf{k} = 0$, we find that the analytic form of the energy spectrum in Eq. (30) is given by

$$E^{(\alpha,\beta)}_{\mathbf{k}} = -\mu_{\mathbf{k}} + \alpha\tilde{\lambda}_{so}(1 + \eta r^2)\sqrt{\sin^2 \mathbf{k}_{3D}} + \beta\sqrt{[m_{\mathbf{k}} + \alpha(1 - \eta r^2)\tilde{\lambda}_{so}\sqrt{\sin^2 \mathbf{k}_{3D}}]^2 + 4r^2\lambda^2_{Ra} \sin^2 \mathbf{k}_{Ra}}, \tag{31}$$

where the anisotropy hopping strength has been considered. Furthermore, we find that $E^{+,\beta}$ remains gapful. Since $E^{(-,+)}_{\mathbf{k}} - E^{(-,-)}_{\mathbf{k}} = 2\sqrt{[m_{\mathbf{k}} - (1 - \eta r^2)\tilde{\lambda}_{so}\sqrt{\sin^2 \mathbf{k}_{3D}}]^2 + 4r^2\lambda^2_{Ra} \sin^2 \mathbf{k}_{Ra}}$, the requirements of $\sin^2 \mathbf{k}_{Ra} = 0$ and $m_{\mathbf{k}} = (1 - \eta r^2)\tilde{\lambda}_{so}\sqrt{\sin^2 \mathbf{k}_{3D}}$ give rise to the condition for the emergence of the Weyl semimetallic phase as

$$\big(\varepsilon_{\mathbf{k}_w} - \varepsilon_\lambda\big)^2 = 4\tilde{\varepsilon}^2_{\tilde{\lambda}_{so}} \sin^2 k_{w_z}, \tag{32}$$

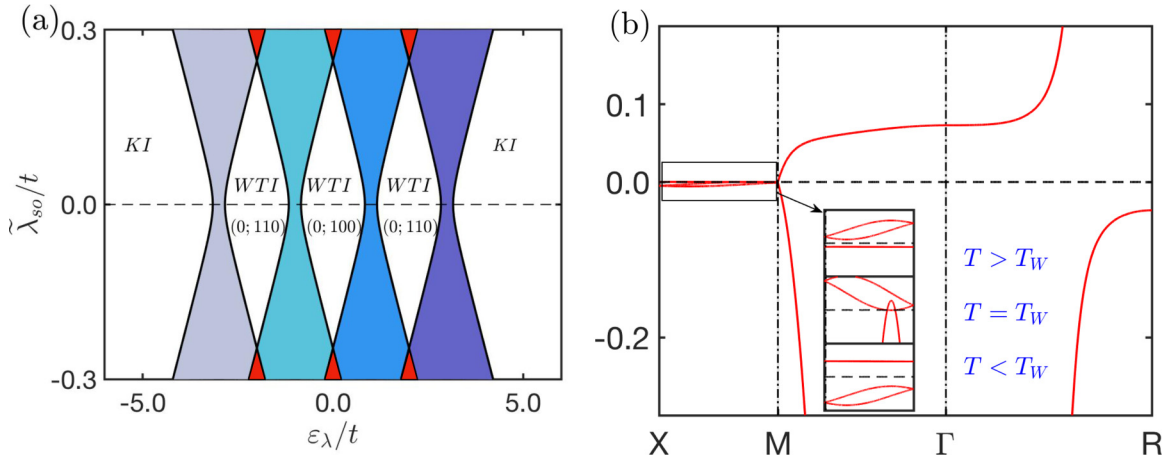

FIG. 5. (a)Topological phase diagram when the inversion symmetry of the Anderson lattice is broken. Here the z axis is the high-symmetry axis, and the anisotropy of the hopping amplitude is characterized by $a_x = 1$, $a_y = 0.5$, $a_z = 0.08$. Here gray, green, blue, and purple regimes are Weyl semimetallic phases with Weyl nodes emerging at $\mathbf{k}_w = (0, 0, k_{w_z})$, $(0, \pi, k_{w_z})$, $(\pi, 0, k_{w_z})$, and (π, π, k_{w_z}), respectively, while the red regime is the overlap regime with the emergence of both Weyl nodes from the overlapping Weyl semimetallic phases. (b) Emergence of the Weyl semimetallic phase at finite temperature. Here Weyl nodes emerge in the k_z axis from X $(\pi, 0, 0)$ to M $(\pi, 0, \pi)$. Note that two intersecting points in the inset may look like a nodal ring. A clear demonstration of these intersecting points being Weyl points is shown in Fig. 6. Parameters are $t = 1$, $\lambda_{so} = 0.2$, $\eta = 0.05$, $\varepsilon_d = 0.705$, $\tilde{\lambda}_{so} = 0.001$, $a_y = 0.5$, and $a_z = 0.001$. The critical temperature for the emergence of Weyl nodes is $T_W = 0.03$.

where the effective parameter that determines the phase boundary is given by $\tilde{\varepsilon}_{\tilde{\lambda}_{so}} = (1 - \eta r^2)\tilde{\lambda}_{so}/(1 + \eta r^2)$. Similarly, solutions to Eq. (30) form the boundary curve between the Weyl semimetallic phase and insulating phases, as illustrated in Fig. 7(a). In addition, solving the mean-field equations, Eqs. (4) and (5), enables one to find that it is possible to tune the Kondo insulator across Weyl semimetallic phases at finite temperatures. As illustrated in Fig. 7(b), the transition occurs at $T_W = 0.03$ when parameters are taken to be $t = 1$, $\lambda_{Ra} = 0.2$, $\eta = 0.05$, $\varepsilon_d = 0.978$, $\tilde{\lambda}_{so} = 0.001$, $a_y = 0.5$, and $a_z = 0.001$. It is seen that the critical temperature for the emergence of Weyl nodes is $T_W = 0.03$. In addition, arranging the linearized form of Eq. (30) in the form of Eq. (13), we find

$$\xi^{\pm}_{\mathbf{k}_w+\mathbf{q}} = \big[-\mu_{\mathbf{k}_w+\mathbf{q}} \pm (1+\eta r^2)K\big]\tau_0 + \big[m_{\mathbf{k}_w+\mathbf{q}} \pm (1-\eta r^2)K\big]\tau_z + 2ir\lambda_{Ra}q_{\pm}\tau_+ + \text{H.c.} \tag{33}$$

It is clear that $\xi^{+}_{\mathbf{k}_w+\mathbf{q}}$ is gapful, while $\xi^{-}_{\mathbf{k}_w+\mathbf{q}}$ can be tuned through the Weyl nodal point. The monopole charge of the emergent Weyl node, however, exhibits charge ± 1 [29], in contrast to the double Weyl node for the case with the hybridization matrix $\mathbf{V}^1_{\mathbf{k}}$.

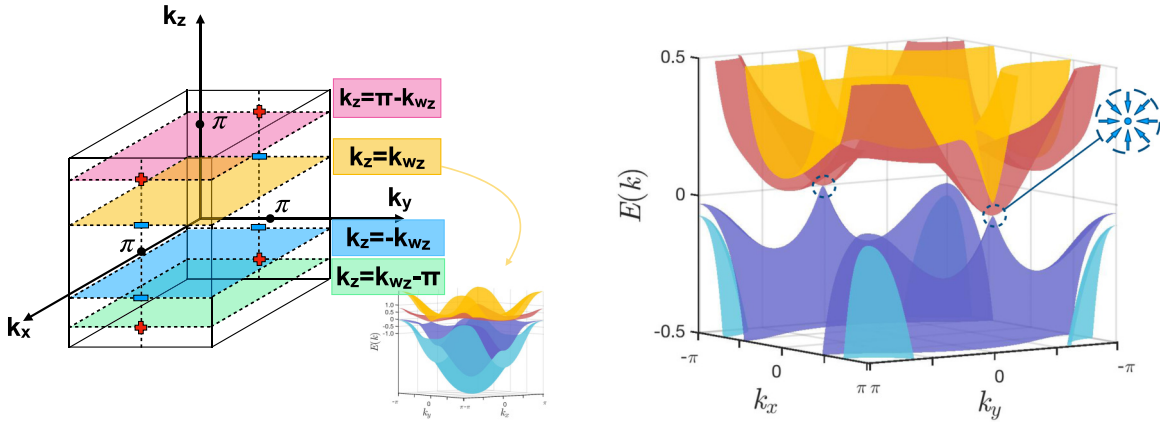

FIG. 6. Sketch of the distribution of Weyl nodes in the first Brillouin zone for Kondo-Weyl semimetals without inversion symmetry. The monopole charge of each Weyl node is $+2$ or -2 and is denoted by $+$ or $-$, respectively. Weyl nodes will move along the dashed lines with changing parameters of the system. Here parameters are $t = 1$, $\lambda_{so} = 0.3$, $\eta = 0.05$, $\varepsilon_d = 1.305$, $\tilde{\lambda}_{so} = 0.3$, $a_y = 0.5$, $a_z = 0.1$, and $T = T_W = 0.03$. Notice that in order to display Weyl nodes clearly, here $E(k)$ does not include the effective chemical potential $\mu_{\mathbf{k}}$.

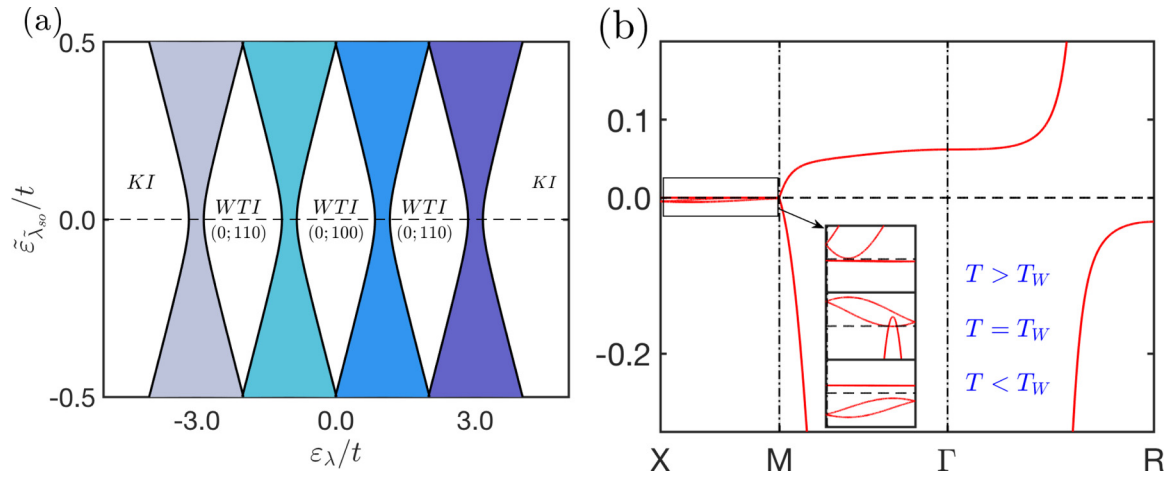

FIG. 7. (a) Topological phase diagram when the hybridization is governed by Rashba interaction. Here the z axis is the high-symmetry axis, and the anisotropy of the hopping amplitude is characterized by $a_x = 1$, $a_y = 0.5$, $a_z = 0.08$. Gray, green, blue, and purple regimes are Weyl semimetallic phases with Weyl nodes emerging at $\mathbf{k}_w = (0, 0, k_{w_z})$, $(0, \pi, k_{w_z})$, $(\pi, 0, k_{w_z})$, and (π, π, k_{w_z}), respectively. (b) Emergence of the Weyl semimetallic phase at finite temperature. Here Weyl nodes emerge in the k_z axis from X $(\pi, 0, 0)$ to M $(\pi, 0, \pi)$. Note that two intersecting points in the inset may look like a nodal ring. A clear demonstration of these intersecting points being Weyl points is confirmed by similar plots shown in Fig. 6. Parameters are $t = 1$, $\lambda_{Ra} = 0.2$, $\eta = 0.05$, $\varepsilon_d = 0.978$, $\tilde{\lambda}_{so} = 0.001$, $a_y = 0.5$, and $a_z = 0.001$. The critical temperature for emergence of Weyl nodes is $T_W = 0.03$.

VI. CONCLUSION AND DISCUSSION

In conclusion, we have demonstrated that by including spin-orbit interactions, topological Weyl semimetallic phases generally emerge from a Kondo insulator upon a change in either temperature or spin-orbit interactions. Two different symmetry classes for the emergent topological semimetallic phases can be realized in the Anderson lattice: the inversion-symmetric semimetallic phase and the time-reversal-invariant semimetallic phase. For the inversion-symmetric semimetallic phase, we found that Weyl nodes appear in pairs with opposite charges (± 1) that are split off from a Dirac node upon broken time-reversal symmetry. On the other hand, we found that the Weyl nodal-ring semimetallic phase generally emerges when the inversion symmetry is broken in the Anderson lattice with general hybridization between the conduction electrons and electrons in the f orbit. Furthermore, when the inversion symmetry is broken through the bulk spin-orbit interaction, two pairs of Weyl nodes emerge together. Depending on the nature of the spin-orbit interaction in the hybridization, the emergent Weyl semimetallic phase can host Weyl nodes with monopole charges of ± 1 or double Weyl nodes with charges of ± 2. All of these topological semimetallic phases are shown to be accessible by tuning either temperature or spin-orbit interactions at an integer filling of 2 [21]. In addition, when the filling of electrons is tuned away from the integer filling for Dirac or Weyl semimetallic phases, the system becomes doped topological semimetals and is a hole Fermi liquid or an electron Fermi liquid, depending on the filling [20]. Furthermore, by tuning the filling, it is expected that the system can be driven through the quantum critical point between the hole Fermi liquid and the electron Fermi liquid or can be driven into the Dirac liquid/Weyl liquid regime [19,20], controlled by the quantum critical point.

While in this work we considered only results based on the slave-boson mean-field theory, we expect that our results are robust qualitatively in the presence of correlation effects as long as the symmetry of the system is not changed. In particular, following Ref. [20], the quasiparticle lifetime τ near the Weyl node can be estimated to be of the order of $\tau^{-1} \sim (\frac{rV_K}{\epsilon_d+\lambda-\mu})^2 \frac{\omega^2+\pi^2(k_BT)^2}{2(\epsilon_d+\lambda-\mu)}$, where $\hbar\omega$ is the energy of the quasiparticle and V_K is the hybridization at the mean-field Fermi momentum. Substituting numerical values, we find that $\epsilon_d + \lambda - \mu \sim 0.02t \sim 1$–$10$ meV and $rV_K \sim 0.002t$. As a result, for quasiparticles with typical energy scales up to 10 meV, $\tau^{-1} \sim 0.1$ meV, and the broadening effect is limited for $k_BT \leqslant 10$ meV. The emergent topological semimetallic phases predicted in this work are thus well defined in finite temperatures up to $k_BT \sim 10$ meV. Our results thus reveal the unusual interplay between the topology of the electronic structures and the Kondo screening in the strongly correlated Anderson lattices and pave the way for systematically engineering topological semimetals based on Kondo lattice systems.

ACKNOWLEDGMENTS

This work was supported by the Ministry of Science and Technology (MoST), Taiwan. We also acknowledge support from the Center for Quantum Technology within the framework of the Higher Education Sprout Project by the Ministry of Education (MOE) in Taiwan.

[1] L. Balents, Physics **4**, 36 (2011).
[2] S. Jia, S.-Y. Xu, and M. Z. Hasan, Nat. Mater. **15**, 1140 (2016).
[3] A. M. Turner and A. Vishwanath, *Beyond Band Insulators: Topology of Semimetals and Interacting Phases* (Elsevier, New York, 2013).

[4] L.-J. Zhai, P.-H. Chou, and C.-Y. Mou, Phys. Rev. B **94**, 125135 (2016).
[5] K. S. Novoselov, A. K. Geim, S. V. Morozov, D. Jiang, Y. Zhang, S. V. Dubonos, I. V. Grigorieva, and A. A. Firsov, Science **306**, 666 (2004).
[6] A. H. Castro Neto, F. A. H. Guinea, N. M. R. Peres, K. S. Novoselov, and A. K. Geim, Rev. Mod. Phys. **81**, 109 (2009).
[7] Z. K. Liu, B. Zhou, Y. Zhang, Z. J. Wang, H. M. Weng, D. Prabhakaran, S.-K. Mo, Z. X. Shen, Z. Fang, X. Dai, Z. Hussain, and Y. L. Chen, Science **343**, 864 (2014).
[8] S. Borisenko, Q. Gibson, D. Evtushinsky, V. Zabolotnyy, B. Buchner, and R. J. Cava, Phys. Rev. Lett. **113**, 027603 (2014).
[9] M. Neupane, Nat. Commun. **5**, 3786 (2014).
[10] S.-Y. Xu, I. Belopolski, N. Alidoust, M. Neupane, G. Bian, C. Zhang, R. Sankar, G. Chang, Z. Yuan, C.-C Lee, S.-M. Huang, H. Zheng, J. Ma, D. S. Sanchez, B. Wang, A. Bansil, F. Chou, P. P. Shibayev, H. Lin, S. Jia, and M. Z. Hasan, Science **349**, 613 (2015); S.-M. Huang, S.-Y. Xu, I. Belopolski, C.-C. Lee, G. Chang, BaoKai Wang, N. Alidoust, G. Bian, M. Neupane, C. Zhang, S. Jia, A. Bansil, H. Lin, and M. Zahid Hasan, Nat. Commun. **6**, 7373 (2015).
[11] L. Lu, Z. Wang, D. Ye, L. Ran, L. Fu, J. D. Joannopoulos, and M. Soljacic, Science **349**, 622 (2015).
[12] B. Q. Lv, H. M. Weng, B. B. Fu, X. P. Wang, H. Miao, J. Ma, P. Richard, X. C. Huang, L. X. Zhao, G. F. Chen, Z. Fang, X. Dai, T. Qian, and H. Ding, Phys. Rev. X **5**, 031013 (2015).
[13] G. Bian, T.-R. Chang, R. Sankar, S.-Y. Xu, H. Zheng, T. Neupert, C.-K. Chiu, S.-M. Huang, G. Chang, I. Belopolski *et al.*, Nat. Commun. **7**, 10556 (2016).
[14] L. M. Schoop, M. N. Ali, C. Straer, A. Topp, A. Varykhalov, D. Marchenko, V. Duppel, S. S. Parkin, B. V. Lotsch, and C. R. Ast, Nat. Commun. **7**, 11696 (2016).
[15] B. J. Yang and N. Nagaosa, Nat. Commun. **5**, 4898 (2014).
[16] A. A. Burkov, M. D. Hook, and L. Balents, Phys. Rev. B **84**, 235126 (2011).
[17] C. Fang, H. Weng, X. Dai, and Z. Fang, Chin. Phys. B **25**, 117106 (2016).
[18] T. Sato, S. Segawa, K. Kosaka, S. Souma, K. Nakayama, K. Eto, T. Minami, Y. Ando, and T. Takahashi, Nat. Phys. **7**, 840 (2011).
[19] D. E. Sheehy and J. Schmalian, Phys. Rev. Lett. **99**, 226803 (2007).
[20] P. H. Chou, L. J. Zhai, C. H. Chung, C. Y. Mou, and T. K. Lee, Phys. Rev. Lett. **116**, 177002 (2016).
[21] J. H. Pixley, S. B. Lee, B. Brandom, and S. A. Parameswaran, Phys. Rev. B **96**, 081105(R) (2017); H. J. Yang and S. B. Lee, arXiv:1810.01451.
[22] M. Dzero, K. Sun, V. Galitski, and P. Coleman, Phys. Rev. Lett. **104**, 106408 (2010).
[23] R. Peters, T. Yoshida, H. Sakakibara, and N. Kawakami, Phys. Rev. B **93**, 235159 (2016).
[24] T. Yoshida, R. Peters, and N. Kawakami, Phys. Rev. B **93**, 045138 (2016).
[25] S. Dzsaber, L. Prochaska, A. Sidorenko, G. Eguchi, R. Svagera, M. Waas, A. Prokofiev, Q. Si, and S. Paschen, Phys. Rev. Lett. **118**, 246601 (2017).
[26] H.-H. Lai, S. E. Grefe, S. Paschen, and Q. Si, Proc. Natl. Acad. Sci. USA **115**, 93 (2018).
[27] F. Teppe, M. Marcinkiewicz, S. S. Krishtopenko, S. Ruffenach, C. Consejo, A. M. Kadykov, W. Desrat, D. But, W. Knap, J. Ludwig, S. Moon, D. Smirnov, M. Orlita, Z. Jiang, S. V. Morozov, V. I. Gavrilenko, N. N. Mikhailov, and S. A. Dvoretskii, Nat. Commun. **17**, 12576 (2016).
[28] A. M. Kadykov, S. S. Krishtopenko, B. Jouault, W. Desrat, W. Knap, S. Ruffenach, C. Consejo, J. Torres, S. V. Morozov, N. N. Mikhailov, S. A. Dvoretskii, and F. Teppe, Phys. Rev. Lett. **120**, 086401 (2018).
[29] C. Fang, M. J. Gilbert, X. Dai, and B. A. Bernevig, Phys. Rev. Lett. **108**, 266802 (2012).
[30] S.-Y. Yang, H. Yang, E. Derunova, S. S. P. Parkin, B. Yan, and M. N. Ali, Adv. Phys. X **3**, 1414631 (2018).
[31] C.-K. Chiu and A. P. Schnyder, Phys. Rev. B **90**, 205136 (2014).
[32] L. Fu, C. L. Kane, and E. J. Mele, Phys. Rev. Lett. **98**, 106803 (2007).